ELSEVIER

Comput. Methods Appl. Mech. Engrg. 190 (2001) 2581–2601

Computer methods in applied mechanics and engineering

www.elsevier.com/locate/cma

High resolution finite-element analysis of shallow water equations in two dimensions

Tony W.H. Sheu *, C.C. Fang

Department of Naval Architecture and Ocean Engineering, National Taiwan University, 73 Chou-Shan Road, Taipei, Taiwan, ROC

Received 15 February 1999; received in revised form 7 January 2000

Abstract

We present in this study the Taylor–Galerkin finite-element model to stimulate shallow water equations for bore wave propagation in a domain of two dimensions. To provide the necessary precision for the prediction of a sharply varying solution profile, the generalized Taylor–Galerkin finite-element model is constructed through introduction of four parameters. This paper also presents the fundamental theory behind the choice of free parameters. One set of parameters is theoretically determined to obtain the high-order accurate Taylor– Galerkin finite-element model. The other set of free parameters is determined using the underlying discrete maximum principle to obtain the low-order monotonic Taylor–Galerkin finite-element model. Theoretical study reveals that the higher-order scheme exhibits dispersive errors near the discontinuity while lower-order scheme dissipates the discontinuity. A scheme which has a high-resolution shock-capturing ability as a built-in feature is, thus, needed in the present study. Notice that lumping of the mass matrix equations is invoked in the low-order scheme to allow simulation of the hydraulic problem with discontinuities. We check the prediction accuracy against suitable test problems, preferably ones for which exact solutions are available. Based on numerical results, it is concluded that the Taylor–Galerkin-flux-corrected transport (TG-FCT) finite-element method can render the technique suitable for solving shallow water equations with sharply varying solution profiles.

1. Introduction

In recent years, there has been considerable interest in environmental problems which have close relevance to the motion of unsteady free-surface flow subjected to gravity forces. Typical examples of these are tides in oceans, breaking waves on shallow beaches, flood waves in rivers, mountain torrents, and estuary flows [1]. In addition, upon sudden opening or closing of a sluice gate and a collapse of hydraulic dams, a bore wave is generated and propagates through the domain. The prediction of the height and speed of the bore has received attention for many years. The knowledge gained can provide useful information for flood control and for the design of channel walls. An observation common to the flows mentioned above is that these flows can be well modeled by shallow water equations. Thus, numerical simulation of shallow water equations was the focus of the present study.

The shallow water equations are the hydraulic analogy of the Euler equations, which govern gas dynamics [1]. The main difference is that contact discontinuity occurs only in gas dynamics. The analogy is rooted in the correspondence between the water elevation h in the shallow water equations and the density in the gas dynamic equations. Given that the Euler differential system for gas dynamics admits discontinuous solutions, called shocks and contact discontinuities, the existing analogy implies the possibility of hydraulic jumps and bores in water and the propagation of a sharp front in the atmosphere. For example,

* Corresponding author. Tel.: +886-2-2362-5470 ext. 246; fax: +886-2-2392-9885.
E-mail address: sheu@indy.na.ntu.edu.tw (T.W.H. Sheu).

0045-7825/01/$ - see front matter
PII: S0045-7825(00)00255-3

the flow of water in a river with a smoothly varying bottom surface may develop into bore waves. As is in the prediction of shocks, numerically capturing discontinuous physical phenomena in hydraulics has become a major area of study both theoretically and computationally.

As alluded to previously, there exists an analogy between the working equations for gas dynamics and those for shallow water. Thus, it is tempting to apply the successful methods so far developed for gas dynamics problems to hydraulic problems governed by the shallow water equations. The MacCormack scheme has gained wider popularity among hydraulic engineers [2]. Due to improper signal transmission, this second-order accurate scheme exhibits dispersive errors near the shock front. The same is true for the other classical high-order schemes. To suppress oscillations evident near the discontinuity, significant effort has been directed towards the development of a monotonic scheme. The idea underpinning modern high-resolution methods in the 1970s originated with Godunov [3] and Van Leer [4]. This was followed by the adoption of the total variation diminishing (TVD) schemes of Harten [5], the flux corrected transport (FCT) methods of Boris and Book [6] and Zalesak [7], the piecewise parabolic method (PPM) of Collela and Woodward [8], and the essentially non-oscillatory (ENO) scheme of Harten and Osher [9] to obtain high-resolution solutions. As in the context of gas dynamics, doubt arose as to whether high-resolution schemes developed essentially on the one-dimensional basis could be extended to multi-dimensional analyses. It is this doubt that has prompted several research endeavors in genuinely multi-dimensional scheme development to capture a bore wave in an open-channel flow and hydraulic jumps in a broken dam [10–19]. Numerical models for this purpose require non-oscillatory schemes with the ability to simulate bore waves accurately while being able to deal with the complex geometry that arises in practice. We consider in this paper the adoption of the Taylor–Galerkin finite-element model. To retain the good shock-capturing property of discontinuous hydraulic solutions, we choose the FCT filtering technique, which was originally developed without resorting to a single spatial dimension [6,7]. To the author's knowledge, this discontinuity-resolving scheme is one of the most suitable choices for multi-dimensional calculations.

The remainder of this paper is organized as follows. Section 2 presents assumptions that lead to the St. Venant shallow water equations, which account for friction losses and bed slopes. The nature of the shallow water is also described in terms of eigenvectors and eigenvalues of the hyperbolic equations. In Section 3, we present the Taylor–Galerkin finite-element model which has the ability to retain faithfully the hyperbolic property that is inherent in the flow conservation law. The key elements that the present finite-element model possesses are the four free parameters and one damping parameter that are introduced into the formulation to achieve higher prediction accuracy in the high-order scheme while accommodating the monotonicity property in the low-order scheme [20]. This is followed by a fundamental study of the finite-element model presented here. Our focus is modified equation analysis, by means of which we can confirm that the numerical model accommodates the desirable consistency property. For stability, we also conduct phase response analysis. It has to be noted that the four free parameters are theoretically determined. No tuning of adjustable parameters is needed, unlike other methods. Section 5 details the flux-corrected transport scheme, by means of which the high-order and low-order Taylor–Galerkin formulations can be used in combination to yield a smooth solution without too much loss of accuracy due to excessive damping added in the vicinity of discontinuities. This section is also intended to provide a theoretical background for the theory of the M-matrix. This underlying theory is important as it provides us guideline to specify values of four free parameters and one damping coefficient. Before going into a discussion of dam-break results, it is highly desirable to check the prediction accuracy of the developed scheme against suitable test problems, preferably ones for which exact solutions are available. In Section 6, we provide analytical evidence that the numerical model is potentially able to render the technique suitable for hydraulic problems with sharp gradients. All results for model tests are in good agreement when compared to the analytic data. With this success in analytical validation, we proceed to study the dam-break problem. We conclude with some remarks in Section 7.

2. Mathematical formulation

We begin this section by presenting the shallow water equations. The equations are an approximation to the full free-surface gravity flow equations with viscosity and surface tension effects neglected. Wind shear

and Coriolis forces are also neglected in the present incompressible flow analysis. For modeling free-surface flows, working equations were usually derived under the assumption of a small bottom slope of the channel. Another key assumption contained in the derivation of St. Venant equations is that the vertical component of the acceleration of the water particle has a negligible influence on the pressure. Hydrostatic pressure distribution is, thus, assumed. The numerical procedure for obtaining the solution to the shallow water equations involves considering mass and momentum conservation in conservative forms as [21]

$$\mathbf{U}_t + \mathbf{F}_x + \mathbf{G}_y = \mathbf{S}. \tag{1}$$

In the above equation, $\mathbf{U}$ represents the solution vector of conservative variables

$$\mathbf{U} = \begin{pmatrix} h \\ hu \\ hv \end{pmatrix}, \tag{2}$$

where h is the depth of the water, and u and v are the depth-averaged velocity components in the x- and y-directions, respectively. Assuming that the diffusion of momenta due to turbulence is negligible and is not included in the equations, the transport of $\mathbf{U}$ in shallow water involves physical fluxes in the x- and y-coordinates, which are derived as

$$\mathbf{F} = \begin{pmatrix} hu \\ hu^2 + \frac{1}{2}gh^2 \\ huv \end{pmatrix}, \tag{3}$$

$$\mathbf{G} = \begin{pmatrix} hv \\ huv \\ hv^2 + \frac{1}{2}gh^2 \end{pmatrix}, \tag{4}$$

where g is the gravitational acceleration.

In Eq. (1), the source term $\mathbf{S}$ accounts for friction losses and bed slopes. Therefore, it is convenient to express $\mathbf{S}$ as

$$\mathbf{S} = \begin{pmatrix} 0 \\ gh(S_{bx} - S_{fx}) \\ gh(S_{by} - S_{fy}) \end{pmatrix}, \tag{5}$$

where S_{fx} and S_{fy} correspond to the friction slopes along the x- and y-directions, respectively. To be able to account for these losses, one can model S_{fx} and S_{fy} by means of constitutive equations, defined as [22]

$$S_{fx} = \frac{n^2 u(u^2 + v^2)^{1/2}}{h^{4/3}}, \tag{6}$$

$$S_{fy} = \frac{n^2 v(u^2 + v^2)^{1/2}}{h^{4/3}}, \tag{7}$$

where n denotes Manning's roughness coefficient. As the name indicates, the bed slopes S_{bx} and S_{by} are defined by $(S_{bx}, S_{by}) = (-\partial h_0/\partial x, -\partial h_0/\partial y)$, where h_0 represents the bed height [19]. To simplify illustration of the method, only the homogeneous case is considered ($\mathbf{S} = \mathbf{0}$) in the present two-dimensional study.

Even for the case in which the initial data is smooth everywhere, the above hyperbolic partial differential equations may admit discontinuities, such as bore waves that are commonly observed in practice, due to non-linear terms in the equations. In seeking to perform time-accurate simulation of these equations, a better understanding of the characteristic nature of the differential system is of considerable importance. It is, thus, customary to rewrite working equations in their equivalent non-conservative form

$$\mathbf{U}_t + \mathbf{A}\mathbf{U}_x + \mathbf{B}\mathbf{U}_y = 0. \tag{8}$$

Equivalence between Eqs. (1) and (8) is retained, provided that

$$\mathbf{A} = \frac{\partial \mathbf{F}}{\partial \mathbf{U}} = \begin{bmatrix} 0 & 1 & 0 \\ -u^2 + c^2 & 2u & 0 \\ -uv & v & u \end{bmatrix}, \tag{9}$$

$$\mathbf{B} = \frac{\partial \mathbf{G}}{\partial \mathbf{U}} = \begin{bmatrix} 0 & 0 & 1 \\ -uv & v & u \\ -v^2 + c^2 & 0 & 2v \end{bmatrix}. \tag{10}$$

The derivation of Eqs. (8)–(10) involves using the velocity of the gravity wave

$$c = (gh)^{1/2}. \tag{11}$$

Like the Euler equations applied in the numerical analysis of compressible gas dynamics, eigenvectors and eigenvalues for **A** and **B** are critical for hydraulic simulation since they correspond to the characteristic speeds and directions of signal transmission. An accurate prediction of propagation phenomena requires knowledge of the characteristic system of hyperbolic equations. To enable information to be transmitted in the correct direction, we derive the eigenvectors e^1, e^2, e^3 for **A** and f^1, f^2, f^3 for **B** as follows:

$$e^1 = (1, u + c, v), \tag{12a}$$
$$e^2 = (0, 0, c), \tag{12b}$$
$$e^3 = (1, u - c, v), \tag{12c}$$
$$f^1 = (1, u, v + c), \tag{12d}$$
$$f^2 = (0, -c, 0), \tag{12e}$$
$$f^3 = (1, u, v - c). \tag{12f}$$

The corresponding eigenvalues a^1, a^2 and a^3 for **A** and b^1, b^2, and b^3 for **B** are obtained as

$$a^1 = u + c, \tag{13a}$$
$$a^2 = u, \tag{13b}$$
$$a^3 = u - c, \tag{13c}$$
$$b^1 = v + c, \tag{13d}$$
$$b^2 = v, \tag{13e}$$
$$b^3 = v - c. \tag{13f}$$

To close the problem, conservation equations are solved subject to initial and boundary conditions discussed later. Our aim with this differential system is to provide detailed information about the flow that would be very expensive to obtain experimentally.

3. Taylor–Galerkin finite-element model

When performing finite-element calculations on hyperbolic equations, we encounter several variants which we can employ to account for the embedded characteristic information. Depending on how the upwinding mechanism is incorporated into the variational statement, there are the characteristic finite-element method and discontinuous finite-element method. Besides these, the characteristic-Galerkin, Petrov–Galerkin, and the Taylor–Galerkin finite-element models are available as alternatives to an accurate unsteady Euler flow simulation. These methods have been used with a great deal of success in the literature. While one model may have advantages over others in some aspects, this is beyond the scope of the present work, and we restrict ourselves here only to the Taylor–Galerkin finite-element model.

The Taylor–Galerkin finite-element model involves performing Taylor series expansion to approximate time derivative terms [23]. This is followed by conducting the Galerkin approximation of the spatial derivatives to complete the formulation. The key property of this model, which renders the technique suitable for hydraulic problems with shocks is the exploitation of Taylor series expansion up to third-order accuracy in time. Higher-order time derivative terms are further transformed to spatial derivatives to obtain not only higher prediction accuracy, but also to stabilize the discrete system through introduction of artificial viscosity.

Using the Galerkin weighted residual approximation method, Eq. (1) can be written in its weak form through the use of test function **W**. This leads to

$$\sum_{el=1}^{n_{el}} \int_{\Omega^{el}} \int_{t_n}^{t_{n+1}} \mathbf{W}\left[\frac{\partial \mathbf{U}}{\partial t}+\frac{\partial \mathbf{F}}{\partial x}+\frac{\partial \mathbf{G}}{\partial y}\right] \mathrm{d}t\, \mathrm{d}\Omega^{el}=0. \tag{14}$$

Define $\delta\mathbf{U}^n=\mathbf{U}^{n+1}-\mathbf{U}^n$ and

$$\mathbf{I}=\frac{\partial}{\partial x}\int_{t_n}^{t_{n+1}} \mathbf{F}\,\mathrm{d}t+\frac{\partial}{\partial y}\int_{t_n}^{t_{n+1}} \mathbf{G}\,\mathrm{d}t.$$

Eq. (14) can be derived as follows through time integration

$$\sum_{el=1}^{n_{el}} \int_{\Omega^{el}} [\mathbf{W}\delta\mathbf{U}^n-\mathbf{W}\mathbf{I}]\,\mathrm{d}\Omega^{el}=0. \tag{15}$$

The analysis is followed by performing Taylor series expansion on the flux terms **F** and **G** with respect to time at t_n. Take **F** as an example, we can approximate this flux by virtue of Taylor series expansion up to the time increment $(t-t_n)^3$

$$\mathbf{F}=\mathbf{F}^n+\left.\frac{\partial \mathbf{F}}{\partial t}\right|^n (t-t_n)+\frac{1}{2}\left.\frac{\partial^2 \mathbf{F}}{\partial t^2}\right|^n (t-t_n)^2+\mathcal{O}(t-t_n)^3. \tag{16}$$

Given that $\partial\mathbf{U}/\partial t=-\mathbf{F}_x-\mathbf{G}_y$ and

$$\frac{\partial \mathbf{F}}{\partial t}=\frac{\partial \mathbf{F}}{\partial \mathbf{U}}\frac{\partial \mathbf{U}}{\partial t}=\mathbf{A}\frac{\partial \mathbf{U}}{\partial t},$$

we can introduce two free parameters α and β to rewrite $\partial\mathbf{F}/\partial t$ as

$$\frac{\partial \mathbf{F}}{\partial t}=\alpha\mathbf{A}\frac{\partial \mathbf{U}}{\partial t}+\beta\mathbf{A}\left[-\frac{\partial \mathbf{F}}{\partial x}-\frac{\partial \mathbf{G}}{\partial y}\right]. \tag{17}$$

It is noted that α and β are constrained by $\alpha+\beta=1$. By virtue of Eq. (17), we can perform the time derivation on $\partial\mathbf{F}/\partial t$ to yield

$$\frac{\partial^2 \mathbf{F}}{\partial t^2}=-\gamma\left(\mathbf{A}^2\frac{\partial^2 \mathbf{U}}{\partial t\partial x}+\mathbf{A}\mathbf{B}\frac{\partial^2 \mathbf{U}}{\partial t\partial y}\right)\Bigg|^n+\mu\left[\mathbf{A}^2\left(\frac{\partial^2 \mathbf{F}}{\partial x^2}+\frac{\partial^2 \mathbf{G}}{\partial x\partial y}\right)+\mathbf{A}\mathbf{B}\left(\frac{\partial^2 \mathbf{F}}{\partial x\partial y}+\frac{\partial^2 \mathbf{G}}{\partial y^2}\right)\right]\Bigg|^n. \tag{18}$$

As before, free parameters which are constrained by $\gamma+\mu=1$ are introduced. Substitution of Eqs. (17) and (18) into Eq. (16) leads to

$$\begin{aligned}\mathbf{F}=\mathbf{F}^n&+\left[\alpha\mathbf{A}\frac{\partial \mathbf{U}}{\partial t}-\beta\mathbf{A}\left(\frac{\partial \mathbf{F}}{\partial x}+\frac{\partial \mathbf{G}}{\partial y}\right)\right]\Bigg|^n (t-t_n)\\&-\frac{1}{2}\left\{\gamma\left(\mathbf{A}^2\frac{\partial^2 \mathbf{U}}{\partial t\partial x}+\mathbf{A}\mathbf{B}\frac{\partial^2 \mathbf{U}}{\partial t\partial y}\right)-\mu\left[\mathbf{A}^2\left(\frac{\partial^2 \mathbf{F}}{\partial x^2}+\frac{\partial^2 \mathbf{G}}{\partial x\partial y}\right)+\mathbf{A}\mathbf{B}\left(\frac{\partial^2 \mathbf{F}}{\partial x\partial y}+\frac{\partial^2 \mathbf{G}}{\partial y^2}\right)\right]\right\}\Bigg|^n (t-t_n)^2\\&+\mathrm{O}((t-t_n)^3),\end{aligned} \tag{19}$$

Similarly, we can expand $\mathbf{G}$ with respect to quantities evaluated at time t_n

$$\mathbf{G} = \mathbf{G}^n + \left[\alpha\mathbf{B}\frac{\partial\mathbf{U}}{\partial t} - \beta\mathbf{B}\left(\frac{\partial\mathbf{F}}{\partial x} + \frac{\partial\mathbf{G}}{\partial y}\right)\right]\Bigg|^n (t-t_n) - \frac{1}{2}\left\{\gamma\left(\mathbf{BA}\left(\frac{\partial^2\mathbf{U}}{\partial t\partial x} + \mathbf{B}^2\frac{\partial^2\mathbf{U}}{\partial t\partial y}\right) - \mu\left[\mathbf{AB}\left(\frac{\partial^2\mathbf{F}}{\partial x^2} + \frac{\partial^2\mathbf{G}}{\partial x\partial y}\right) + \mathbf{B}^2\left(\frac{\partial^2\mathbf{F}}{\partial x\partial y} + \frac{\partial^2\mathbf{G}}{\partial y^2}\right)\right]\right\}\Bigg|^n (t-t_n)^2 + \mathrm{O}((t-t_n)^3). \tag{20}$$

It is the four free parameters built into this formulation that make the present analysis more suitable for providing high- and low-order solutions. By substituting Eqs. (19) and (20) into Eq. (15) and choosing bilinear polynomials as test and basis functions, we can derive the finite-element equation in operator form

$$\mathbf{M}\delta\mathbf{U}^n = \mathbf{R}, \tag{21}$$

where the vector $\mathbf{R}$ is expressed by

$$\mathbf{R} = \mathbf{C}\mathbf{F}^n + \tilde{\mathbf{C}}\mathbf{G}^n. \tag{22}$$

Full details of the operators shown in Eq. (22) are summarized in Appendix A. In Eq. (21), the consistent mass matrix $\mathbf{M}$ is as follows:

$$\mathbf{M} = \mathscr{A}_{el=1}^{n_{el}}\left[\mathbf{M}_{ij}^{el}\right], \tag{23}$$

where

$$M_{ij}^{el} = \int_{\Omega^{el}}\left\{\mathbf{N}_i\mathbf{N}_j - \frac{1}{2}\alpha\Delta t\left(\frac{\partial\mathbf{N}_i}{\partial x}A + \frac{\partial\mathbf{N}_i}{\partial y}B\right)\mathbf{N}_j + \frac{1}{6}\gamma\Delta t^2\left[\frac{\partial\mathbf{N}_i}{\partial x}\left(A^2\frac{\partial\mathbf{N}_j}{\partial x} + AB\frac{\partial\mathbf{N}_j}{\partial y}\right) + \frac{\partial\mathbf{N}_i}{\partial y}\left(BA\frac{\partial\mathbf{N}_j}{\partial x} + B^2\frac{\partial\mathbf{N}_j}{\partial y}\right)\right]\right\}\mathrm{d}\Omega^{el} - \int_{\Gamma}\left\{-\frac{1}{2}\alpha\Delta t\mathbf{N}_i\left(n_xA + n_yB\right)\mathbf{N}_j + \frac{1}{6}\gamma\Delta t^2\mathbf{N}_i\left[n_x\left(A^2\frac{\partial\mathbf{N}_j}{\partial x} + AB\frac{\partial\mathbf{N}_j}{\partial y}\right) + n_y\left(BA\frac{\partial\mathbf{N}_j}{\partial x} + B^2\frac{\partial\mathbf{N}_j}{\partial y}\right)\right]\right\}\mathrm{d}\Gamma. \tag{24}$$

When it comes to capturing discontinuous profiles at which numerical instabilities often set in, direct calculation of $\delta\mathbf{U}$ from the matrix equation (21) may not be successful. For stability reasons, it is convenient to lump the matrix. This is followed by adding artificial damping terms into the formulation. This implies that it is more rational to work with the following lower-order Taylor–Galerkin finite-element model:

$$\bar{\mathbf{M}}\delta\mathbf{U}^n = \mathbf{R} + \mathbf{D}, \tag{25}$$

where the lumping mass matrix $\mathbf{M}$ is as follows:

$$\bar{\mathbf{M}} = \mathscr{A}_{el=1}^{n_{el}}\left(\mathrm{diag}\left(\sum_{j=1}\mathbf{M}_{ij}^{el}\right)\right). \tag{26}$$

In Eq. (25), the damping vector $\mathbf{D}$ is chosen as

$$\mathbf{D} = c_d(\mathbf{M} - \bar{\mathbf{M}})\mathbf{U}^n. \tag{27}$$

Determination of c_d is critical to the prediction of a sharp wave profile and forms one part of our research effort aimed at providing the ability to capture at discontinuous profiles.

When simulating supercritical shallow water equations, one finds that locally sonic flow may be encountered. In such circumstances, entropy fix is required to avoid rarefraction shock near the sonic point [24]. To obtain the scheme which accommodates the entropy satisfaction property, we add the damping terms

$$\frac{\partial}{\partial x}\left(b(v_x)\frac{\partial\mathbf{U}}{\partial x}\right) + \frac{\partial}{\partial y}\left(b(v_y)\frac{\partial\mathbf{U}}{\partial y}\right)$$

into the continuity equation. The damping coefficient we consider in this study is given by

$$b(v_i) = c_e \frac{\Delta t}{2\lambda^2} q(v_i), \tag{28}$$

where

$$q(v_i) = \begin{cases} 0, & |v_i| \geqslant \epsilon, \\ \epsilon^2 - v_i^2, & |v_i| < \epsilon, \end{cases} \tag{29}$$

and

$$v_i = \frac{\Delta t}{\Delta x}(u - c) \quad \left(\text{or } v_i = \frac{\Delta t}{\Delta y}(v - c)\right). \tag{30}$$

In the above, u, v are the velocity components in the x- and y-directions, respectively. As for c, it is denoted as the wave speed. Free parameter shown in Eqs. (28)–(30) are given by $\epsilon = 0.2$ and $c_e = 2.0$.

4. Fundamental study on the Taylor–Galerkin finite-element model

4.1. High-order Taylor–Galerkin finite-element model

A full understanding of the approximation scheme requires knowledge of the phase error and amplification factor of the scheme. To simplify the analysis, we use a model equation which bears resemblance to the working equations. This model equation is the pure convection equation, which involves constant speeds a and b as follows:

$$\phi_t + f_x + g_y = \phi_t + a\phi_x + b\phi_y = 0. \tag{31}$$

Following the approach discussed in the previous section, we can transform Eq. (31) into its discrete form akin to the finite-difference equation. In the nine-point compact stencils, the discrete representation for the model equation in a domain with uniform grid size is

$$\sum a_{ij} \delta \mathbf{U}_{ij}^n = \sum b_{ij} \mathbf{U}_{ij}^n. \tag{32}$$

The expressions for a_{ij} and b_{ij} are written in terms of Courant numbers v_x ($\equiv a\Delta t/\Delta x$) and v_y ($\equiv b\Delta t/\Delta y$). They are detailed in Appendix B for the reader's reference.

Having derived the coefficient of the discrete equation, we can conduct the modified equation analysis. The idea behind this analysis is rooted in Taylor series expansion. By making use of Taylor series expansion, we can derive the modified equation, in the terminology of warming and Hyett [25], as follows:

$$\begin{aligned} \phi_t + a\phi_x + b\phi_y = {} & (\alpha + \beta - 1)\left(\frac{1}{2} vx\Delta x a\phi_{xx} + v_x \Delta x b\phi_{xy} + \frac{1}{2} v_y \Delta y b\phi_{yy}\right) \\ & + \frac{1}{12}(2 - 3\alpha - 2\gamma)\left(v_x^2 (\Delta x)^2 a\phi_{xxx} + v_y^2 (\Delta y)^2 b\phi_{yyy}\right) \\ & + \frac{1}{12}(-9\alpha - 6\gamma - 4\mu + 6)\left(v_x^2 (\Delta x)^2 b\phi_{xxy} + v_y^2 (\Delta y)^2 a\phi_{xyy}\right) \\ & + T_1\phi_{xxxx} + T_2\phi_{xxxy} + T_3\phi_{xxyy} + T_4\phi_{xyyy} + T_5\phi_{yyyy} + \cdots, \end{aligned} \tag{33}$$

where

$$T_1 = \frac{1}{24}a^2\Delta t\Delta x^2\Big[(2\alpha+\beta-2)+v_x^2(2\alpha+2\gamma-1)\Big], \tag{34a}$$

$$T_2 = \frac{1}{6}ab\Delta t\Delta x^2\Big[(\alpha+\beta-1)+v_x^2(2\alpha+2\gamma-1)\Big], \tag{34b}$$

$$T_3 = \frac{1}{12}\frac{\Delta x^2\Delta y^2}{\Delta t}\Big[(\alpha+\beta-1)+(v_x^2+v_y^2)+v_x^2v_y^2(6\alpha+2\gamma-3)\Big], \tag{34c}$$

$$T_4 = \frac{1}{6}ab\Delta t\Delta y^2\Big[(\alpha+\beta-1)+v_y^2(2\alpha+2\gamma-1)\Big], \tag{34d}$$

$$T_5 = \frac{1}{24}b^2\Delta t\Delta y^2\Big[(2\alpha+\beta-2)+v_y^2(2\alpha+2\gamma-1)\Big]. \tag{34e}$$

Although the algebra needed to obtain the above modified equation is considerable, Eqs. (34a)–(34e) can provide insights into the dissipation and dispersion errors for the numerical scheme considered here. In the light of Eq. (33), the modified equation provides us with a well-established basis for legitimate control of free parameters α, β, γ and μ. Imposing $\alpha+\beta=1$, we can eliminate the leading even-derivative term. Following the same line, we can also eliminate the leading dispersion error, provided that the coefficients of the third-order derivatives ϕ_{xxx} and ϕ_{yyy} are zero. This leads to

$$2-3\alpha-2\gamma=0. \tag{35}$$

The above two equations enable us to assign values to α, β, γ and μ a priori to obtain a higher-order scheme. It is easy to see that the choice of $\alpha=\mu=0,\ \beta=\gamma=1$ makes the rest of the third-order derivatives zero and leads to

$$\phi_t + a\phi_x + b\phi_y = T_1\phi_{xxxx} + T_2\phi_{xxxy} + T_3\phi_{xxyy} + T_4\phi_{xyyy} + T_5\phi_{yyyy} + \cdots \tag{36}$$

With continuous refinement of the grid sizes, the discretization errors approach zero. This shows that the present discretization scheme accommodates the desired consistency property. It is now worthwhile to point out that the present Taylor–Galerkin approach has no adjustable parameter. In the light of the higher level of spatial accuracy presented here, the underlying numerical scheme shows promise as a tool in the prediction of the smooth water height in shallow water equations.

In hydraulic simulation of shallow water wave propagation, phase error will certainly occur. Thus, care must be taken to retain the inherent non-dispersive characteristics. With this understanding, it is clear that what is of critical importance in the water wave prediction is its close relation with the phase velocities of all the waves supported by the medium governed by the linearized Euler equations. Pursuit of high-order accuracy in phase is thus requisite. According to Donea et al. [26], better phase accuracy can be obtained using the Taylor–Galerkin finite-element model. The improved phase accuracy is due to the inclusion of a higher-order term in the Taylor series expansion. The leading dispersion error arising from the spatial and temporal discretizations is, thus, eliminated.

Conducting phase response analysis amounts to computing the ratio of the semi-discrete phase velocity Φ_{TG} to the exact phase velocity Φ_{exact}

$$r_\Phi = \frac{\Phi_{\mathrm{TG}}}{\Phi_{\mathrm{exact}}}. \tag{37}$$

Considering the model equation (31) defined in two dimensions, the exact phase velocity (or frequency), namely $\Phi_{\mathrm{exact}} = -\Delta t((a,b)(q_x,q_y))$, is obtained as

$$\Phi_{\mathrm{exact}} = \Phi_0 e^{\mathrm{i}(q_x(x-at)+q_y(y-bt))}, \tag{38}$$

where q_x and q_y denote the wave numbers along the x- and y-directions, respectively. In the case of uniform grid spacing $\Delta x=\Delta y=h$, we can normalize the wave number vector by

$$\xi = (\xi, \eta) = (hq_x, hq_y). \tag{39}$$

We now examine how the computed phase velocity varies with the flow direction. To achieve this goal, we rewrite the velocity vector as a function of $\theta \equiv \tan^{-1} b/a$

$$(a, b) = (a^2 + b^2)^{1/2}(\cos\theta, \sin\theta). \tag{40}$$

According to von Neumann stability analysis (or Fourier analysis), we can derive the amplification factor G and phase velocity Φ_{TG} for the proposed scheme given by (32)

$$G = \frac{V_1 + V_3 + \mathrm{i}(V_2 + V_4)}{V_1 + \mathrm{i}V_2} = \text{function}(|\xi|, \theta), \tag{41}$$

$$\Phi_{\mathrm{TG}} = \tan^{-1}\left(\frac{V_1 V_4 - V_2 V_3}{V_1^2 + V_2^2 + V_1 V_3 + V_2 V_4}\right), \tag{42}$$

where

$$\begin{aligned} V_1 = {} & \left[\frac{4}{9} + \frac{2}{9}\gamma(v_x^2 + v_y^2)\right] + \left[\frac{2}{9} - \frac{1}{9}\gamma(2v_x^2 - v_y^2)\right]\cos\xi + \left[\frac{1}{18} - \frac{1}{18}\gamma(v_x^2 + 3v_x v_y + v_y^2)\right]\cos(\xi + \eta) \\ & + \left[\frac{2}{9} + \frac{1}{9}\gamma(v_x^2 - 2v_y^2)\right]\cos\eta + \left[\frac{1}{18} + \frac{1}{18}\gamma\big(-v_x^2 + 3v_x v_y - v_y^2\big)\right]\cos(-\xi + \eta), \end{aligned} \tag{43a}$$

$$V_2 = \frac{1}{3}\alpha v_x \sin\xi + \frac{1}{12}\alpha\big(v_x + v_y\big)\sin(\xi + \eta) + \frac{1}{3}\alpha v_y \sin\eta + \frac{1}{12}\alpha\big(-v_x + v_y\big)\sin(-\xi + \eta), \tag{43b}$$

$$\begin{aligned} V_3 = {} & \left[-\frac{2}{3}\beta(v_x^2 + v_y^2)\right] + \left[\frac{1}{3}\beta(2v_x^2 - v_y^2)\right]\cos\xi + \left[\frac{1}{6}\beta(v_x^2 + 3v_x v_y + v_y^2)\right]\cos(\xi + \eta) \\ & + \left[\frac{1}{3}\beta(-v_x^2 + 2v_y^2)\right]\cos\eta + \left[\frac{1}{6}\beta(v_x^2 - 3v_x v_y + v_y^2)\right]\cos(-\xi + \eta), \end{aligned} \tag{43c}$$

$$\begin{aligned} V_4 = {} & \left[-\frac{2}{3}v_x + \frac{2}{3}\mu v_x v_y^2\right]\sin\xi + \left[-\frac{1}{6}(v_x + v_y) - \frac{1}{3}\mu v_x v_y (v_x + v_y)\right]\sin(\xi + \eta) \\ & + \left[-\frac{2}{3}v_y + \frac{2}{3}\mu v_x^2 v_y\right]\sin\eta + \left[-\frac{1}{6}(-v_x + v_y) + \frac{1}{3}\mu v_x v_y(-v_x + v_y)\right]\sin(-\xi + \eta). \end{aligned} \tag{43d}$$

While it is a complicated matter to conduct phase response analysis, this fundamental analysis helps to reveal that the value of r_Φ depends on the wavelength, $\lambda = 2\pi h/|\vec{\xi}|$, and on the direction of the propagation wave, θ. To provide justification for the use of the present scheme, we have plotted r_Φ at different values of the wavelength in Fig. 1. Noticeable is a significant improvement of the scheme over the Lax–Wendroff scheme in terms of isotropy.

4.2. Monotonic Taylor–Galerkin finite-element model

Despite the fact that the use of $\alpha = \mu = 0,\ \beta = \gamma = 1$ provides a third-order accurate method for solving Eq. (31), the lack of the monotonicity property has been known to give rise to post-shock oscillations. A detailed exposition of the free parameters $\alpha, \beta, \gamma, \mu$ and c_d must show how to provide good control of these parameters in order to accurately resolve sharp gradient profiles. Among the few methodologies in existence, we adopt the theory of the M-matrix to suppress oscillations near discontinuities [27].

Before embarking on a systematic treatment of the problem, it is desirable to present here the theory of the M-matrix. A real $n \times n$ matrix $\mathbf{A} = (a_{ij})$ is defined as being irreducible diagonally dominant if there exists at least one i such that $|a_{ii}| > \sum_{j=1, j\neq i}^{n} |a_{ij}|$. According to the theorem, if a real, irreducible diagonally dominant matrix accommodates the property $a_{ij} \leqslant 0$ for $i \neq j$ and $a_{ii} > 0$ for $1 \leqslant i \leqslant n$, then this matrix is invertible. Also, the inverse of $\mathbf{A}$ has no negative entries. We call such a matrix an M-matrix. Presented

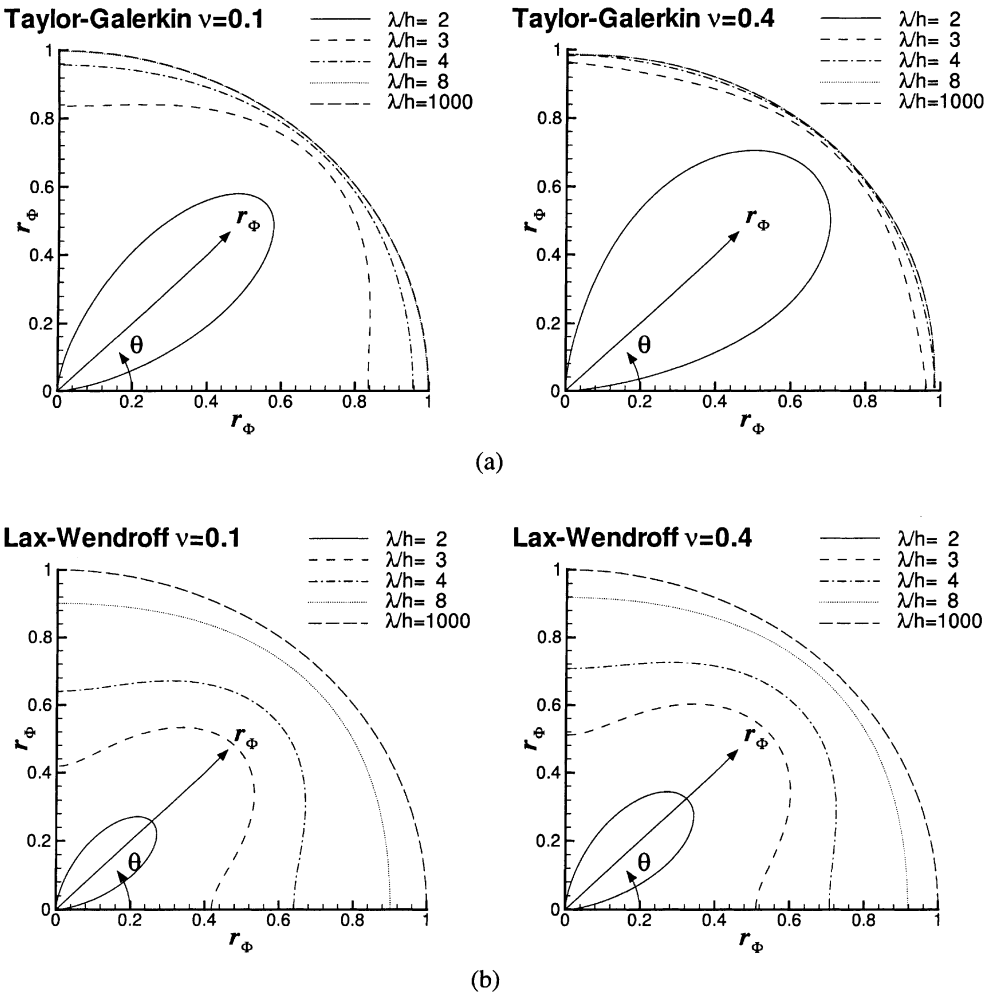

Fig. 1. The plot of r_Φ against λ/h and v: (a) the scheme developed in this paper; (b) Lax–Wendroff scheme.

below are one definition and one theorem that provide us with a theoretical basis for constructing the low-order Taylor–Galerkin scheme, which has the monotonic property [27].

Definition. A real $n \times n$ matrix $\mathbf{A}$ is monotonic if $\mathbf{A}\phi \geqslant 0$ for any vector ϕ, then $\phi > 0$.

Theorem. *If the off-diagonal entries of* $\mathbf{A}$ *are non-positive, then this matrix is called monotonic if and only if* $\mathbf{A}$ *is an* M*-matrix.*

Thanks to the theory of the M-matrix, which provides guidelines for the design of an M-matrix in the stencil points shown in Eq. (32), we are able to construct a stiffness matrix of the M-matrix type by assigning values of the free parameters. Throughout this study, $(\alpha, \beta, \gamma, \mu, c_d) = (0, 0, 0, 0, 1.5)$ is used to provide low-order monotonic solutions.

5. Flux-corrected transport filtering algorithm

Despite the widespread use of upwind schemes to resolve problems with dominant convection flux terms, spurious oscillations are seen in the vicinity of discontinuities. To overcome this difficulty, researchers have

resorted to developing monotonic schemes to capture flow discontinuities in a non-oscillatory way. In the present work, we employ the flux-correct transport technique to suppress oscillations evident near discontinuities. The FCT solution algorithm of Boris and Book [6] was recognized as the first monotonic positivity-preserving technique and was later generalized by Zalesak [7]. The idea behind the algorithm is to combine a high-order accurate scheme with a low-order scheme. To be effective, we demand that the former scheme be used in the smooth regime and the low-order scheme only in regions near discontinuities. It is noteworthy that the chosen filtering scheme should be applicable to multi-dimensional analyses. The key property that explains why the scheme can resolve high-gradient solutions is the incorporation of a monotonic scheme, as discussed in Section 4.2, into the formulation. Thus far, two sets of values $(\alpha, \beta, \gamma, \mu, c_d)$ have been shown to yield high- and low-order accurate finite-element solutions.

We now turn to using two Taylor–Galerkin schemes in combination to provide a high-resolution capturing scheme. The idea behind the use of two schemes in combination is the flux-correct transport scheme of Zalesak [7]. This scheme involves introducing an anti-diffusive flux array $\mathbf{F}^{el^h}$, which is computed based on the high-order accurate Taylor–Galerkin solutions, into each element. With solutions of $\delta\mathbf{U}^h$, we can compute the anti-diffusive flux array $\mathbf{F}^{el^h} = [F_i^{el^h}] = \bar{\mathbf{M}}_h^{-1}[\mathbf{R}^{el^h} - (\mathbf{M}^{el^h} - \bar{\mathbf{M}}^{el^h})\delta\mathbf{U}^h]$. The analysis is followed by computing the anti-diffusive flux array $\mathbf{F}^{el^l}$ based on the low-order Taylor–Galerkin finite-element solutions. Given the legitimate free parameters $(\alpha^l, \beta^l, \gamma^l, \mu^l, c_d^l)$, we can compute $\delta\mathbf{U}^l$ using the lumping-mass method to yield $\delta\mathbf{U}^l$. With values of $\delta\mathbf{U}^l$ already computed, we can compute the anti-diffusive flux array in each element as $\mathbf{F}^{el^l} = [\bar{\mathbf{M}}^{-1}\mathbf{R}^{el^l}]$. Having obtained anti-diffusive fluxes $\mathbf{F}^{el^h}$ and $\mathbf{F}^{el^l}$, we can compute the flux array $\mathbf{F}^{el}$ from

$$F_i^{el} = \bar{\mathbf{M}}_h^{-1}\left[\mathbf{R}_i^{el^h} - \left(\mathbf{M}_{ij}^{el^h} - \bar{\mathbf{M}}_i^{el^h}\delta_{ij}\right)\delta\mathbf{U}_j^h\right] - \bar{\mathbf{M}}_l^{-1}\mathbf{R}_i^{el^l}. \tag{44}$$

Following the major steps given in the FCT algorithm of Zalesak [7], we need to estimate two extreme values $U_I^{\max}$ and $U_I^{\min}$ defined in each element Ω^{el}:

$$U_I^{\max} = \max\left(U_{el}^a|_{I\in\Omega^{el},\forall el}\right), \tag{45}$$

$$U_I^{\min} = \min\left(U_{el}^b|_{I\in\Omega^{el},\forall el}\right), \tag{46}$$

where $I \in \Omega^{el}$ denotes the global number I within each Ω^{el}. In Eqs. (45) and (46), U_{el}^a and U_{el}^b are expressed as $U_{el}^a = \max(U_I^a|_{I\in\Omega^{el},\forall I})$ and $U_{el}^b = \min(U_I^b|_{I\in\Omega^{el},\forall I})$, where $U_I^a = \max(U_I^n, U_I^l)$ and $U_I^b = \max(U_I^n, U_I^l)$. We then calculate Q_I^+ and Q_I^- from $Q_I^+ = U_I^{\max} - U_I^l$ and $Q_I^- = U_I^{\min} - U_I^l$, respectively. This is followed by calculating P_I^+ and P_I^-, whose values are related to the anti-diffusive fluxes shown in Eq. (44):

$$P_I^+ = \mathscr{A}_{el=1}^{n_{el}}\left(\max\left(0, F_i^{el}\right)\right), \tag{47}$$

$$P_I^- = \mathscr{A}_{el=1}^{n_{el}}\left(\min\left(0, F_i^{el}\right)\right). \tag{48}$$

We then calculate the ratios of $Q_I^\pm/P_I^\pm$, from which the estimation of R_I^+ and R_I^- is obtained

$$R_I^+ = \begin{cases} \min\left(1, Q_I^+/P_I^+\right), & P_I^+ \neq 0, \\ 0, & P_I^+ = 0, \end{cases} \tag{49}$$

$$R_I^- = \begin{cases} \min\left(1, Q_I^-/P_I^-\right), & P_I^- \neq 0, \\ 0, & P_I^- = 0. \end{cases} \tag{50}$$

Execution of the algorithm is followed by determination of C_i^{el} as given below

$$C_i^{el} = \begin{cases} \min\left(R_I^+|_{I\in\Omega^{el}}\right), & F_i \geqslant 0, \\ \min\left(R_I^-|_{I\in\Omega^{el}}\right), & F_i < 0. \end{cases} \tag{51}$$

At this point, we can correct the anti-diffusive flux F_i^{el} by multiplying it by C_i^{el} just derived. The resulting corrected anti-diffusive flux array F^{elc} reads as

$$F_i^{elc} = C_i^{el} F_i^{el}. \tag{52}$$

The filtering processes are completed with the calculation of $\mathbf{U}^{n+1}$ as

$$\mathbf{U}^{n+1} = \mathbf{U}^{l} + \mathscr{A}_{el=1}^{n_e l}\left(\mathbf{F}^{elc}\right), \tag{53}$$

where

$$\mathbf{F}^{elc} = \left[F_i^{elc}\right]. \tag{54}$$

6. Numerical results

Before any computational result can be deemed reliable for use in engineering practice, the numerical model must be validated. To provide justification for the validity and usefulness of the Taylor–Galerkin-flux-corrected transport (TG-FCT) finite-element model, we consider here test problems which are amenable to analytic solutions.

6.1. Verification of the TG-FCT finite-element model

In this paper, we consider a scalar transport equation in the specified flow. A feature of the analytic solution of the test problem is its apparently discontinuous solution profile. The problem under investigation is shown schematically in Fig. 2. In the square, defined in the range $0 \leqslant x,\ y \leqslant 1$, a sharp scalar profile is set as the initial condition. The centroid of the cylindrically configured profile is located at $(0.25, 0.5)$. This initially discontinuous scalar profile is transported in the flow domain, within which the flow velocity is of the rotating type: $u = -y + 0.5,\ v = x - 0.5$. Rectangular Cartesian grids are uniformly overlaid on the region of interest. Given grid sizes of $\Delta x = \Delta y = 1/100$, the time increment for this study is

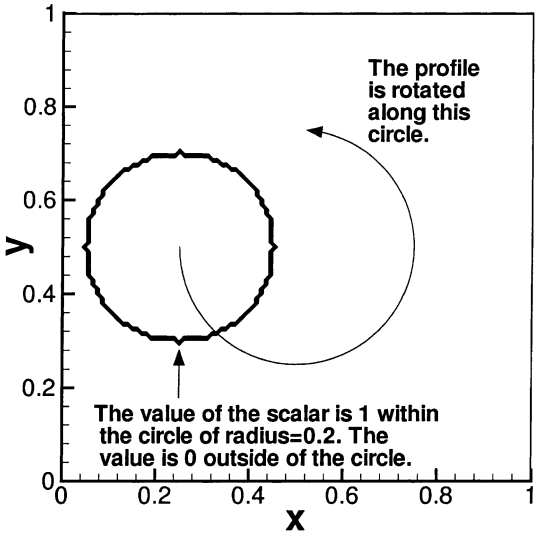

Fig. 2. The initial conditon for the problem considered in Section 6.1.

chosen to be $\Delta t = \pi/800$. Depending on the velocity magnitude $\bar{u} = ((x-0.5)^2 + (0.5-y)^2)^{\frac{1}{2}}$ the Courant numbers involved in this calculation fall within the range of $0 \leqslant v(\equiv \bar{u}\Delta t/\Delta x) < 0.28$. The calculation is terminated at $t = 2\pi$. Numerical evidence, as shown in Fig. 3, clearly indicates that the field variable is well predicted without observable oscillations. This result serves as a validation for the computational technique, thus showing that the scheme adopted here has the ability to resolve discontinuities.

The next problem is intended to test the ability of the scheme to resolve discontinuous field variables in the gas dynamic equations. The problem under investigation concerns the gas dynamics, which have been studied by Lax as a model problem [28]. We seek a solution in a square domain within which the initial conditions are schematically shown in Fig. 4. The results are presented for a case with grid spacing at $\Delta x = \Delta y = h = 1/99$. Starting with the initial data for u, v, and ρ, equations governing the gas dynamics were solved in a domain, which has been uniformly discretized. The Courant number is set to be 0.25. Fig. 5

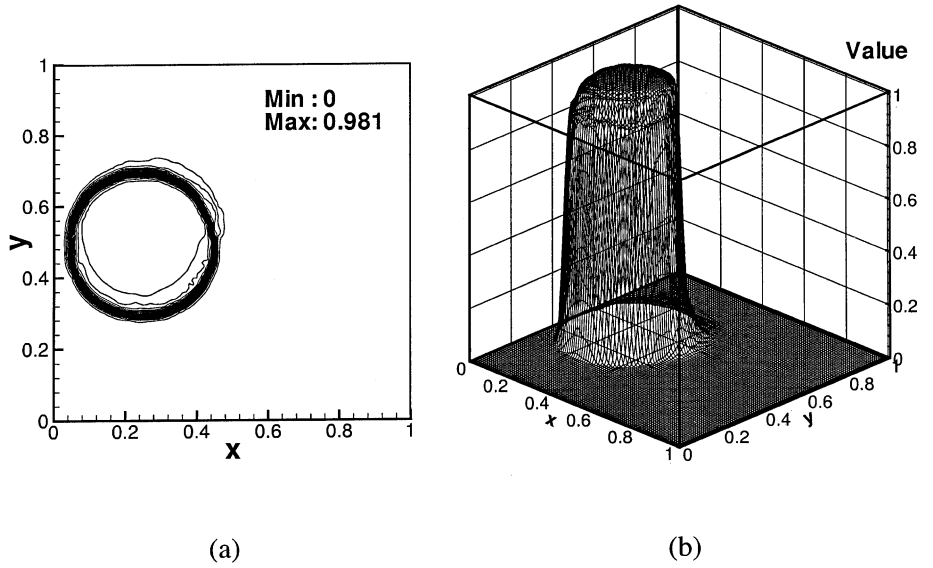

Fig. 3. The computed solution after one cycle of rotation for the problem considered in Section 6.1: (a) contour plot; (b) three-dimensional view of the computed solution.

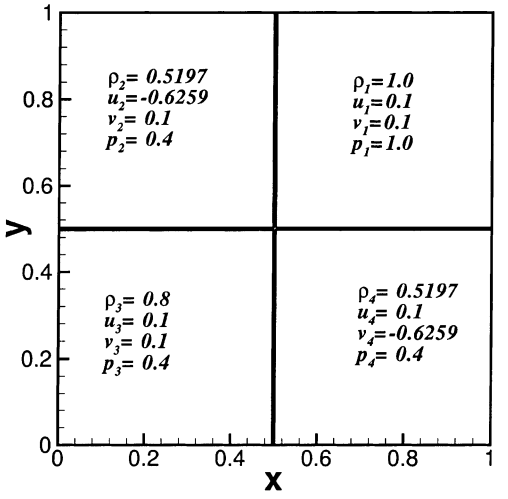

Fig. 4. The initial condition for the gas dynamics problem considered in Section 6.1.

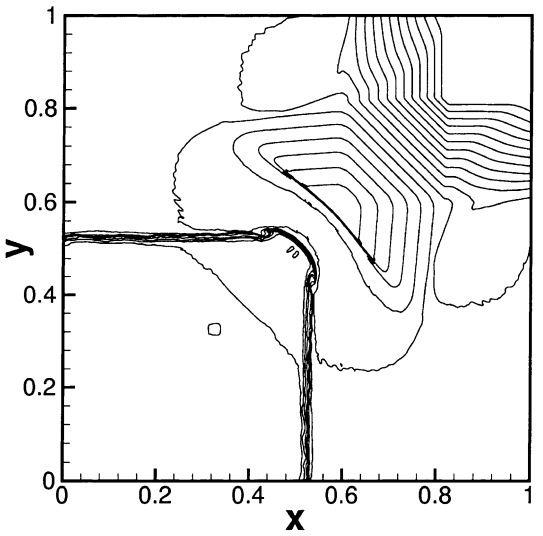

Fig. 5. The computed density contours for the problem considered in Section 6.1.

shows that the computed contours of density at $t = 0.25$ are fully characterized by sharply changed solution profiles. The predicted density contours are seen to agree favorably with the data of Lax [28]. The same holds true for other results not shown here.

6.2. Analytic verification of the TG-FCT finite-element model for solving shallow water equations in two dimensions

Having analytically verified the proposed finite-element model, we can proceed to apply this computationally efficient scheme to solve problems governed by shallow water equations. We consider here the time-evolving water surface elevation in a basin, inside which a dam is partially broken. As a first step toward predicting wave propagation in a partially failed dam, we consider a one-dimensional dam-break problem using the proposed two-dimensional finite-element code. The problem is schematically shown in Fig. 6. This problem is modeled in order to allow comparison of our results with analytically available solutions. The test problem consists of a dam of length 100 m. For the present study, a channel 300 m long and 100 m wide is discretized into 1201×7 grids for numerical calculation. The case under

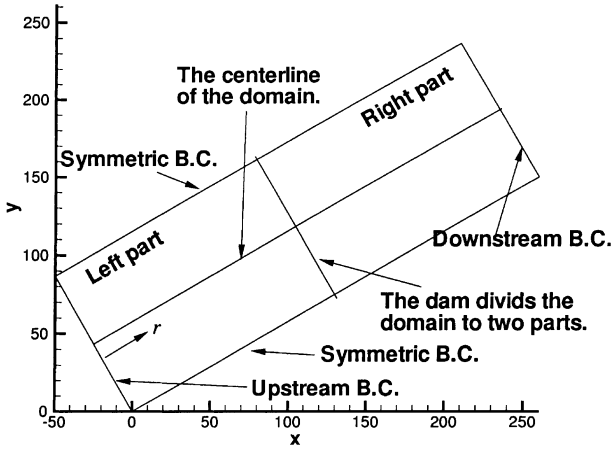

Fig. 6. A schematic illustration of the problem considered in Section 6.2.

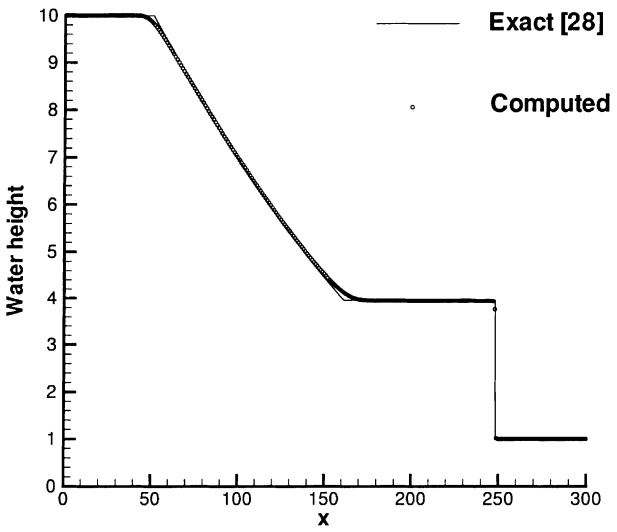

Fig. 7. A comparison of the computed and analytic solutions for the problem considered in Section 6.2.

investigation is a subcritical flow with a water-height ratio of 10. Both the upstream and downstream boundary conditions remain unchanged during the calculation. For this purpose, the test is run and terminated at $t = 10$ s.

As Fig. 7 shows, our result compares very favorably with the analytic data due to Stoker [29] given below

$$h(\tilde{x},t) = \begin{cases} h_1 & \text{if } \tilde{x}/t \leqslant -\sqrt{gh_1}, \\ \frac{1}{9_g}\left[2\sqrt{gh_1} - \frac{\tilde{x}}{t}\right]^2 & \text{if } -\sqrt{gh_1} < \tilde{x}/t \leqslant [u_m - \sqrt{gh_m}], \\ h_m & \text{if } [u_m - \sqrt{gh_m}] < \tilde{x}/t \leqslant s, \\ h_2 & \text{if } s < \tilde{x}/t \leqslant \infty. \end{cases} \tag{55}$$

In the above, $\tilde{x} = x - x_0$, where x_0 is the location of the discontinuity. As for h_m and u_m, they are two constant values for the water height and the velocity in the middle state of this problem. Their values are related to the propagation speed of the shock s given below:

$$h_m = \frac{1}{2}\left[\sqrt{1 + \frac{8s^2}{gh_2}} - 1\right]h_2, \tag{56}$$

$$u_m = s - \frac{gh_2}{4s}\left[1 + \sqrt{1 + \frac{8s^2}{gh_2}}\right]. \tag{57}$$

The shock speed s is determined from the positive real root of the following equation:

$$u_m + 2\sqrt{gh_m} - 2\sqrt{gh_1} = 0. \tag{58}$$

Fig. 8 plots the evolution of fluid flow with time. At the plane of symmetry, it is clearly seen that there are two waves: one travels to the left and the other to the right. The left-running family of rarefraction (or

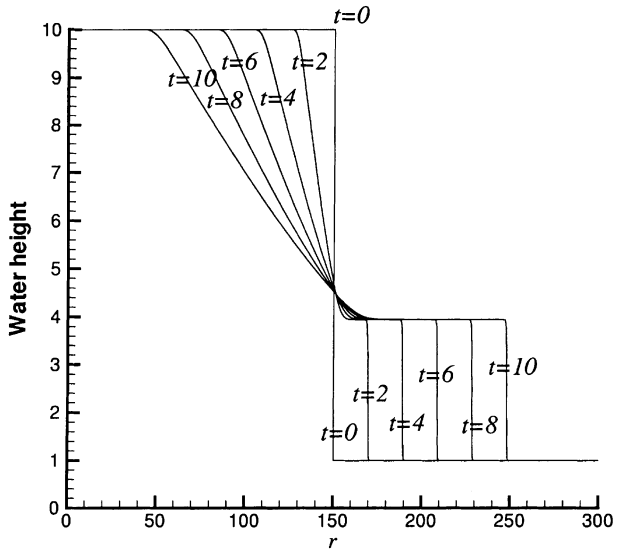

Fig. 8. The time-evoluting water heights for the problem conisdered in Section 6.2.

depression) waves and the right-running shock (or bore) create three constant states, which are accurately predicted. In the left fan-like rarefraction waves, one encounters the locally sonic flow. To avoid unphysical rarefraction shocks at the sonic point $x = 150$, the entropy flux term, discussed in Section 3, is invoked to retain the entropy satisfaction property. Also revealed from this figure is the shock wave, which is well resolved within very few grid points without post-shock oscillations evident in the solution. The improved accuracy is clearly seen near discontinuity. This test demonstrates that the FCT technique built into the Taylor–Galerkin formulation has the ability to suppress dispersive errors near the discontinuity, without adding dissipation errors to the smooth flow. Also, the entropy flux added to the high-order Taylor–Galerkin finite-element model has been shown very effective to suppress the unphysical entropy glitch at the sonic point.

6.3. Prediction of water surface elevation in a partially failed dam problem

The analysis is followed by considering a basin of simplified geometry. At the midpoint of the square basin, 200 m long, there is a dam, as is shown schematically in Fig. 9, which divides the water in two parts.

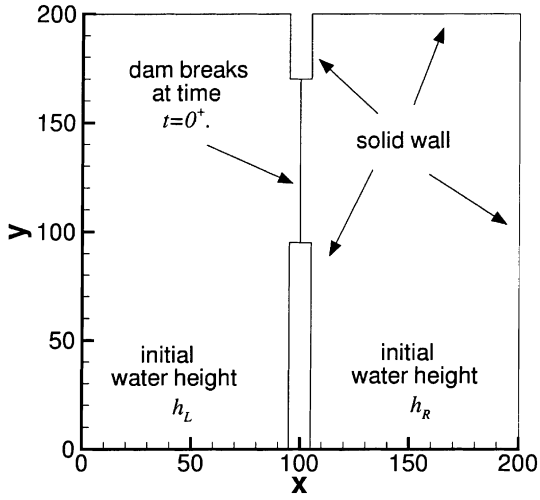

Fig. 9. A schematic illustration of the problem considered in Section 6.3.

The dam has a width of 10 m. On both sides of this dam, the water elevations maintain a height ratio other than 1. The Courant number is chosen to be 0.1, and the grid has uniform spacing $\Delta x = \Delta y = 2.5$. At time $t = 0^+$, the dam is partially broken, leading to a breach with a width of 75 m. The flow pattern resulting from this partially breached dam depends on whether it is subcritical or supercritical. The case examined here is a subcritical flow with $h_L/h_R = 2$, where $h_L(\equiv 10\text{ m})$ denotes the initial water elevation on the left side of the basin, while $h_R(\equiv 5\text{ m})$ represents the water height on the right side. Given that the ratio h_L/h_R has a value other than 1, water is released into the downstream side through the breach, which is located in the range of $95\text{ m} \leqslant y \leqslant 170\text{ m}$. A direct consequence of this dam failure is a bore wave, which propagates forward and spreads laterally. At the same time, a negative depression wave spreads upstream. In addition, a standing wave forms due to the reduction in velocity at the two side walls. The calculation is terminated at

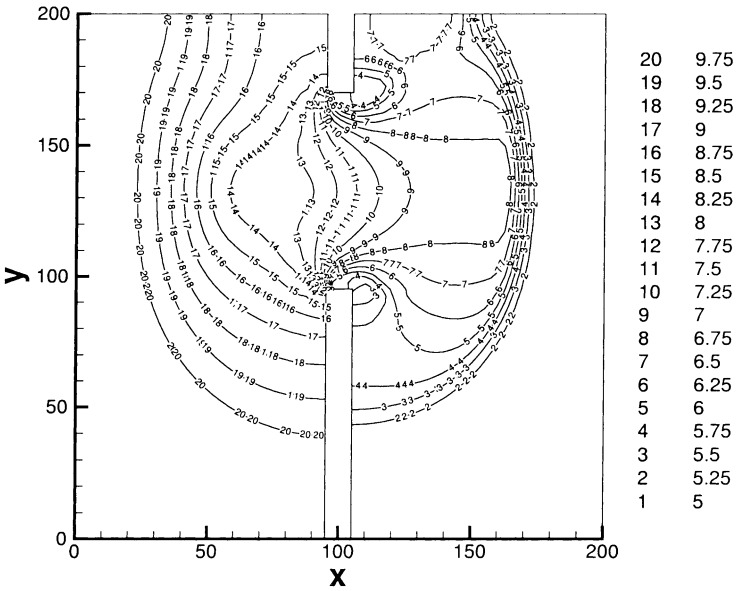

Fig. 10. The contours of water height for the partial dam-break problem considered in Section 6.3.

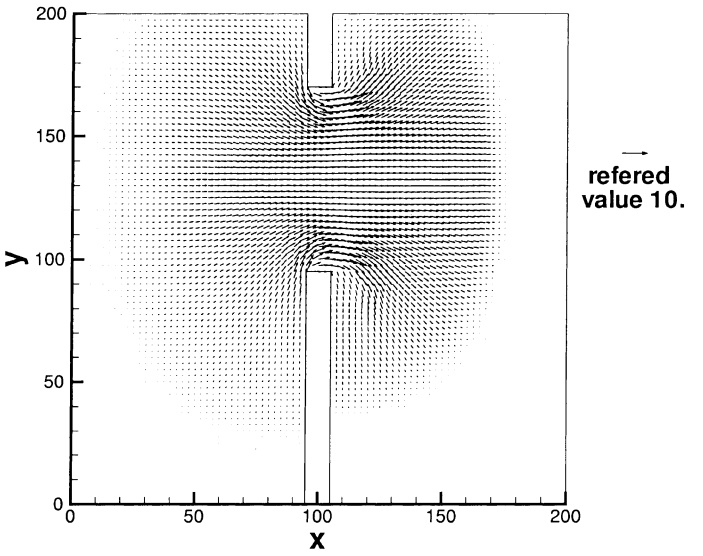

Fig. 11. The velocity plot for the partial dam-break problem considered in Section 6.3.

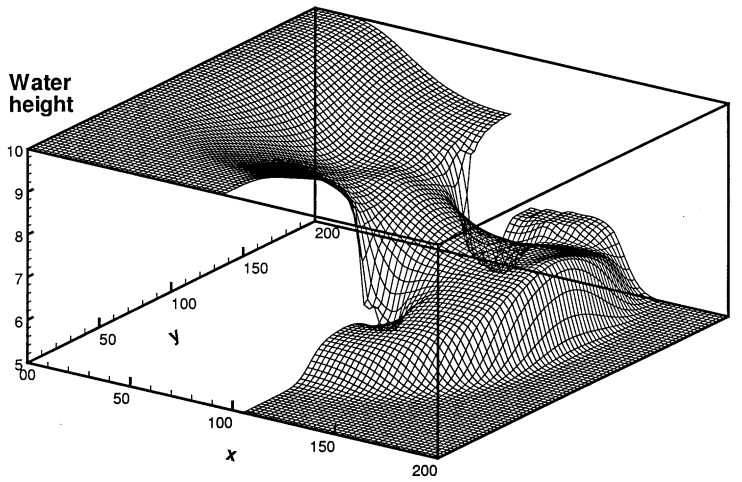

Fig. 12. The three-dimensional view of the water elevation for the partial dam-break problem considered in Section 6.3.

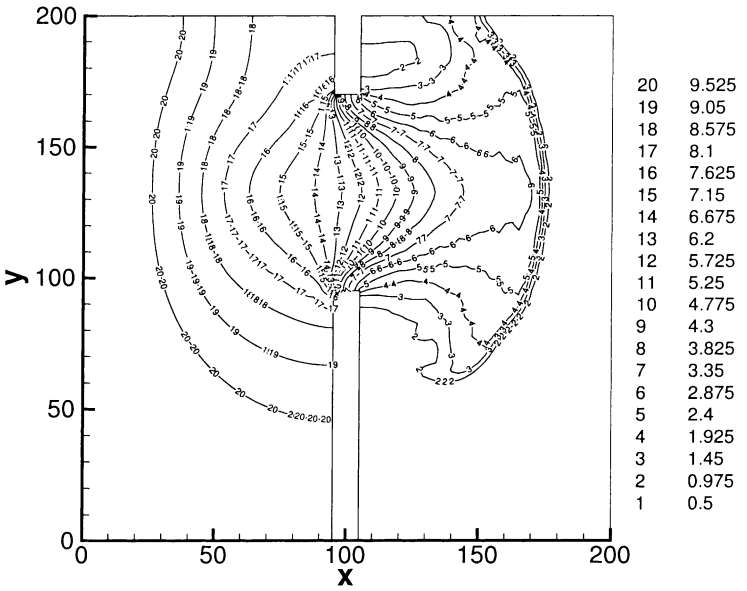

Fig. 13. The contour plot of the water elevation for the partial dam-break problem with an initial value of $h_R/h_L = 0.05$.

time $t = 7.2$ s. Our goal is to numerically predict the propagation and spreading of the wave with time into the reservoir.

Fig. 10 plots the contour values of the water elevation in the basin. Clearly revealed by this figure is the predicted right traveling bore wave and left traveling depression wave. The ability of the FCT scheme to capture sharp solutions is clearly demonstrated in view of the abrupt depression of the water surface elevation in the vicinity of the breach edge. The manifestation of this sharp depression wave is theoretically justifiable since strong rarefractions are established in the inviscid flow regime where large velocity gradients appear. In light of this fact, we plot in Fig. 11, the velocity vector to show the sharp depression in the water surface elevation around the edges of the breach. From this velocity vector plot, we are led to conclude that the regions of large velocity gradients observed near the edges of the breach appear to be those which are most subject to abrupt depressions in the water surface elevation. For a clear presentation of the solution, we plot in Fig. 12 a three-dimensional view of the water surface

elevation after the dam breaks. As this figure shows, this problem is a demanding test for the hydrodynamic numerical simulation.

To show that the method proposed here can handle severely changed solution profiles with very little loss of prediction accuracy, we also consider a supercritical flow. The initially prescribed water height ratio is $h_R/h_L = 0.05$. As Fig. 13 shows, water heights have been captured in a sharp and non-oscillatory way.

7. Concluding remarks

A generalized finite-element model formulated within the Taylor–Galerkin framework has been presented to simulate shallow water equations in two dimensions. Two models, which were developed from the generalized Taylor–Galerin model using two different sets of free parameters, have been employed to render the technique suitable for hydraulic problems with sharply varying solution. Free parameters built into the two models, which are the main ingredients of the flux-corrected transport filtering scheme, have been theoretically determined. The goal obtaining the free parameters is to improve the accuracy of the higher-order Taylor–Galerkin model. We adopt modified equation analysis as the underlying methodology in the development of the high-order Taylor–Galerkin scheme. The choice of free parameters for the low-order Taylor–Galerkin model is based on the theory of the M-matrix. Besides four free parameters, another damping coefficient is introduced to facilitate the construction of an M-matrix that allows for the prediction of a solution profile in a sharp and non-oscillatory way. The method based on the FCT formulation manifests many properties desirable in solving shallow water equations, which admit discontinuous solutions. The avoidance of numerical oscillations near the discontinuity and the achievement of higher-order solution accuracy in the smooth region make this scheme a robust tool for solving differential equations governing open channel flows. Extensive test have been performed to study the method's performance on several test problems with particular attention paid to its shock-capturing ability. For the sake of validation, we have checked the prediction accuracy against test problems, choosing ones for which exact solutions are available. These include one for the scalar equation and another for the Euler equations governing gas dynamics. With success in analytically verifying the code, the TG-FCT finite-elements model has been further applied to solving shallow water equations containing an initially sharp change of the water elevation. Field variables have been captured in a sharp and non-oscillatory way for both subcritical and supercritical cases.

Acknowledgements

The authors would like to thank the Computer Center of National Taiwan University and the National Center for High-performance Computing (NCHC) for providing computers CRAY J916 and IBM SP2 computers, which made this study possible. This work is supported by the National Science Council of Republic of China, NSC 88-2611-E-02-025.

Appendix A

We summarize here the expressions of operators shown in Eq. (22):

$$C_{ij}^{el} = \int_{\Omega^{el}} \frac{\partial \mathbf{N}_i}{\partial x}\left[\Delta t \mathbf{N}_j - \frac{1}{2}\beta\Delta t^2\left(A\frac{\partial \mathbf{N}_j}{\partial x} + B\frac{\partial \mathbf{N}_j}{\partial y}\right) + \frac{1}{6}\mu\Delta t^3\left(A^2\frac{\partial^2 \mathbf{N}_j}{\partial x^2} + AB\frac{\partial^2 \mathbf{N}_j}{\partial x\partial y} + BA\frac{\partial^2 \mathbf{N}_j}{\partial x\partial y} + B^2\frac{\partial^2 \mathbf{N}_j}{\partial y^2}\right)\right] \mathrm{d}\Omega^{el} - \int_{\Gamma} n_x \mathbf{N}_i\left[\Delta t \mathbf{N}_j - \frac{1}{2}\beta\Delta t^2\left(A\frac{\partial \mathbf{N}_j}{\partial x} + B\frac{\partial \mathbf{N}_j}{\partial y}\right) + \frac{1}{6}\mu\Delta t^3\left(A^2\frac{\partial^2 \mathbf{N}_j}{\partial x^2} + AB\frac{\partial^2 \mathbf{N}_j}{\partial x\partial y} + BA\frac{\partial^2 \mathbf{N}_j}{\partial x\partial y} + B^2\frac{\partial^2 \mathbf{N}_j}{\partial y^2}\right)\right] \mathrm{d}\Gamma, \tag{A.1}$$

$$\tilde{C}_{ij}^{el} = \int_{\Omega^{el}} \frac{\partial \mathbf{N}_i}{\partial x}\left[\Delta t \mathbf{N}_j - \frac{1}{2}\beta\Delta t^2\left(A\frac{\partial \mathbf{N}_j}{\partial x} + B\frac{\partial \mathbf{N}_j}{\partial y}\right) + \frac{1}{6}\mu\Delta t^3\left(A^2\frac{\partial^2 \mathbf{N}_j}{\partial x^2} + AB\frac{\partial^2 \mathbf{N}_j}{\partial x\partial y} + BA\frac{\partial^2 \mathbf{N}_j}{\partial x\partial y} + B^2\frac{\partial^2 \mathbf{N}_j}{\partial y^2}\right)\right] \mathrm{d}\Omega^{el} - \int_{\Gamma} n_y \mathbf{N}_i\left[\Delta t \mathbf{N}_j - \frac{1}{2}\beta\Delta t^2\left(A\frac{\partial \mathbf{N}_j}{\partial x} + B\frac{\partial \mathbf{N}_j}{\partial y}\right) + \frac{1}{6}\mu\Delta t^3\left(A^2\frac{\partial^2 \mathbf{N}_j}{\partial x^2} + AB\frac{\partial^2 \mathbf{N}_j}{\partial x\partial y} + BA\frac{\partial^2 \mathbf{N}_j}{\partial x\partial y} + B^2\frac{\partial^2 \mathbf{N}_j}{\partial y^2}\right)\right] \mathrm{d}\Gamma. \tag{A.2}$$

Appendix B

We summarize here the coefficients shown in Eq. (32):

$$a_{ij} = \frac{4}{9} + \frac{2}{9}\gamma(v_x^2 + v_y^2), \tag{B.1}$$

$$a_{i+1,j} = \frac{1}{9} + \frac{1}{6}\alpha v_x - \frac{1}{18}\gamma(2v_x^2 - v_y^2), \tag{B.2}$$

$$a_{i+j,j+1} = +\frac{1}{36} + \frac{1}{24}\alpha(v_x + v_y) - \frac{1}{36}\gamma(v_x^2 + 3v_x v_y + v_y^2), \tag{B.3}$$

$$a_{i,j+1} = \frac{1}{9} + \frac{1}{6}\alpha v_y + \frac{1}{18}\gamma(v_x^2 - 2v_y^2), \tag{B.4}$$

$$a_{i-1,j+1} = \frac{1}{36} - \frac{1}{24}\alpha(v_x - v_y) + \frac{1}{36}\gamma(-v_x^2 + 3v_x v_y - v_y^2), \tag{B.5}$$

$$a_{i-1,j} = \frac{1}{9} - \frac{1}{6}\alpha v_x - \frac{1}{18}\gamma(2v_x^2 - v_y^2), \tag{B.6}$$

$$a_{i-1,j-1} = \frac{1}{36} - \frac{1}{24}\alpha(v_x + v_y) + \frac{1}{36}\gamma(v_x^2 + 3v_x v_y + v_y^2), \tag{B.7}$$

$$a_{i,j-1} = \frac{1}{9} - \frac{1}{6}\alpha v_y + \frac{1}{18}\gamma(v_x^2 - 2v_y^2), \tag{B.8}$$

$$a_{i+1,j-1} = \frac{1}{36} + \frac{1}{24}\alpha(v_x - v_y) + \frac{1}{36}\gamma(-v_x^2 + 3v_x v_y - v_y^2), \tag{B.9}$$

$$b_{i,j} = -\frac{2}{3}\beta(v_x^2 + v_x^2), \tag{B.10}$$

$$b_{i+1,j} = -\frac{1}{3}v_x + \frac{1}{6}\beta(2v_x^2 - v_y^2) + \frac{1}{3}\mu v_x v_y^2, \tag{B.11}$$

$$b_{i+1,j+1} = -\frac{1}{12}(v_x + v_y) + \frac{1}{12}\beta(v_x^2 + 3v_x v_y + v_y^2) - \frac{1}{6}\mu v_x v_y(v_x + v_y), \tag{B.12}$$

$$b_{i,j+1} = -\frac{1}{3}v_y + \frac{1}{6}\beta(-v_x^2 + 2v_y^2) + \frac{1}{3}\mu v_x^2 v_y, \tag{B.13}$$

$$b_{i-1,j+1} = \frac{1}{12}(v_x - v_y) + \frac{1}{12}\beta(v_x^2 - 3v_x v_y + v_y^2) - \frac{1}{6}\mu v_x v_y(-v_x + v_y), \tag{B.14}$$

$$b_{i-1,j} = \frac{1}{3}v_x + \frac{1}{6}\beta(2v_x^2 - v_y^2) - \frac{1}{3}\mu v_x v_y^2, \tag{B.15}$$

$$b_{i-1,j-1} = \frac{1}{12}(v_x + v_y) + \frac{1}{12}\beta(v_x^2 + 3v_x v_y + v_y^2) + \frac{1}{6}\mu v_x v_y(v_x + v_y), \tag{B.16}$$

$$b_{i,j-1} = \frac{1}{3}v_y + \frac{1}{6}\beta(-v_x^2 + 2v_y^2) - \frac{1}{3}\mu v_x^2 v_y, \tag{B.17}$$

$$b_{i+1,j-1} = \frac{1}{12}(-v_x + v_y) + \frac{1}{12}\beta(v_x^2 - 3v_x v_y + v_y^2) + \frac{1}{6}\mu v_x v_y(v_x + v_y). \tag{B.18}$$

References

[1] E.F. Toro, Riemann problems and the WAF method for solving the two-dimensional shallow water equations, Philos. Trans. R. Soc. Lond. A 338 (1992) 43–68.
[2] R.W. MacCormack, The effect of viscosity in hypervelocity impact cratering, AIAA paper, Cincinnati, Ohio, 1969, pp. 69–354.
[3] S.K. Godunov, Finite-difference method for numerical computation of discontinuous solutions of the equations of fluid dynamics, Mat. Sb. 147 (1959) 271–306.
[4] B. Van Leer, Towards the ultimate conservative difference scheme, II, monotonicity and second-order combined in a second-order scheme, J. Comput. Phys. 14 (1973) 357–393.
[5] A. Harten, High-resolution schemes for hyperbolic conservation laws, J. Comput. Phys. 49 (1983) 357–393.
[6] J.P. Boris, D.L. Book, Flux corrected transport, SHASTA, a fluid transport algorithm that works, J. Comput. Phys. 11 (1973) 38–69.
[7] S.T. Zalesak, Fully multidimensional flux-corrected transport algorithms for fluids, J. Comput. Phys. 31 (1979) 335–362.
[8] P. Collela, P.R. Woodward, The piecewise parabolic method (PPM) for gas dynamics simulation, J. Comput. Phys. 54 (1984) 174–201.
[9] A. Harten, S. Osher, Uniformly high order accurate non-oscillatory schemes, SIAM 24 (1987) 279–310.
[10] P. Garcia-Navaroo, M.E. Hubband, A. Priestley, Genuinely multidimensional upwinding for the 2D shallow water equations, J. Comput. Phys. 121 (1995) 79–93.
[11] H. Paillere, G. Dergez, H. Deconinck, Multidimensional upwind schemes for the shallow water equations, Int. J. Numer. Methods Fluids 26 (1998) 987–1000.
[12] T. Molls, F. Molls, Space-time conservation method applied to Saint Venant equations, J. Hydr. Engrg., ASCE 124 (5) (1998) 501–508.
[13] C.G. Mingham, D.M. Causon, High-resolution finite-volume method for shallow water flows, J. Hydr. Engrg., ASCE 124 (6) (1998) 605–614.
[14] R.J. Fernema, M.H. Chaudhry, Explicit methods for 2-D transient free-surface flows, J. Hydr. Engrg., ASCE 116 (8) (1990) 1013–1034.
[15] L. Fraccarollo, E. Toro, Experimental and numerical assessment of the shallow water model for two dimensional dam-break type problems, J. Hydr. Res., 33 (6) (Delft, the Netherlands, 1995) 843–864.
[16] R. Garcia, R. Kahawita, Numerical solution of the St. Venant equations with MacCormack finite-difference scheme, Int. J. Numer. Methods in Fluids 6 (1986) 507–527.
[17] D.H. Zhao, H.W. Shen, J.S. Lai, G.Q. Tabios, Approximate Riemann solvers in FVM for 2D hydraulic wave modeling, J. Hydr. Engrg., ASCE 122 (12) (1996) 692–702.
[18] N.D. Katopodes, T. Theodor Strelkoff, Computing two-dimensional dam-break flood waves, J. Hydr. Div., ASCE 104 (1978) 1269–1288.
[19] G. Hauke, A symmetric formulation for computing transient shallow water flows, Comput. Methods Appl. Mech. Engrg. 163 (1998) 111–122.
[20] T.W.H. Sheu, C.C. Fang, A numerical study of nonlinear propagation of disturbances in two-dimensions, J. Comput. Acoustics 4 (3) (1996) 291–319.
[21] M.H. Chaudhry, Open-Channel Flow, Prentice-Hall, Englewood Cliffs, NJ, 1993.
[22] M.H. Hsu, W.H. Teng, C. Lai, Numerical simulation of supercritical shock wave in channel contraction, Computers & Fluids 27 (1998) 347–365.
[23] J. Donea, A Taylor–Galerkin method for convective transport problems, Int. J. Numer. Methods Engrg. 20 (1984) 101–119.
[24] A. Harten, P.D. Lax, B. Van Leer, On upstream differencing and Godunov-type schemes for hyperbolic conservation laws, SIAM Rev. 25 (1983) 35–61.
[25] R.F. Warming, B.J. Hyett, The modified equation approach to the stability and accuracy analysis of finite difference methods, J. Comput. Phys. 14 (1974) 159–179.
[26] J. Donea, Generalized Galerkin methods for convection dominated transport phenomena, Appl. Mech. Rev. 44 (5) (1991) 205–214.
[27] T. Meis, U. Marcowitz, Numerical Solution of Partial Differential Equations, Applied Mathematical sciences, Vol. 32, Springer, New York, 1981.
[28] P.D. Lax, X.D. Liu, Solution of two-dimensional Riemann problems of gas dynamics by positive schemes, SIAM J. Sci. Comput. 19 (1998) 319–340.
[29] J.J. Stoker, Water Waves, Interscience, New York, 1957.